Advances in Science and Technology Research Journal, 2026, 20(1), 14–29 https://doi.org/10.12913/22998624/208491 ISSN 2299-8624, License CC-BY 4.0

Effect of Mo addition on the oxidation behavior of the AlCoCrFeNi high entropy alloy

Wojciech Jerzy Nowak^{1*}, Jakub Jopek¹, Natalia Maciaszek¹

- ¹ Faculty of Mechanical Engineering and Aeronautics, Rzeszow University of Technology, Powstanców Warszawy 12, 35-959 Rzeszów, Poland
- * Corresponding author's e-mail: wjnowak@prz.edu.pl

ABSTRACT

Materials used in the energy sector or in aviation must possess a good combination of mechanical properties and oxidation resistance. These materials face harsh conditions i.e. high temperature and oxidative atmospheres. This leads to severe degradation of the materials. To overcome this problem, protective coatings are applied. However, this introduces additional costs. Therefore, a new solution is required. Therefore, a relatively new kind of alloys, which are high entropy alloys, are of interest of many researchers. In the present work, AlCoCrFeNi high entropy alloys doped with Mo in the amount ranging between 0–5 at.% were investigated to elucidate the effect of Mo addition on the AlCoCrFeNi-xMo microstructure, microhardness and high temperature oxidation resistance. It was found that the increase in Mo content leads to ordering the microstructure from lamellar, in the case of reference alloy, to mosaic in the case of HEA containing 4 and 5 at.% of Mo. For the latter, a significant increase in microhardness was found and correlated directly with changes in microstructure. However, oxidation tests revealed that an increase in Mo, in addition to HEA, worsens the oxidation resistance of the studied materials. This phenomenon was explained by a more severe spallation of the alumina scale and the subsequent increased formation of internal Al nitrides. The reaction of Al with N-entrapped Al lowers Al content to a level below the critical Al content for transformation from the internal scale to the external scale formation.

Keywords: high entropy alloys, high temperature corrosion, oxidation resistance.

INTRODUCTION

Currently, research is focused on developing new types of materials to satisfy the increasing requirements of the modern industry [1-3]. Often, enhancing process efficiency involves creating advanced metal alloys [4, 5]. This approach is especially crucial in the aerospace sector, where material technologies are among the factors limiting the performance of aircraft gas turbines [6]. Nickel-based superalloys with thermal barrier coatings (TBCs) are widely used in aircraft engines operating in extreme conditions, serving to protect metal substrates from oxidation at high temperatures [7, 8] and creep resistance [9]. Despite notable improvements in their durability, these components can still suffer damage due to factors such as high temperature corrosion [6, 10–13]. The challenge of overcoming these material limitations drives ongoing intensive development efforts [1, 14–16].

Received: 2025.07.18

Accepted: 2025.09.22

Published: 2025.11.21

An alternative to traditional alloys is offered by high entropy alloys (HEA), which are based on fundamentally different principles [17–20]. HEA typically comprises five elements, each with a concentration ranging from 5% to 35 atomic percent, along with minor dopant additions (up to 5 at.%). A notable subgroup of HEA includes those based on elements such as Al, Co, Cr, Fe, and Ni. These alloys can be produced through methods such as arc melting, mechanical alloying, plasma spraying, magnetron sputtering, laser alloying [21, 22], or powder metallurgy [23]. For example, AlCoCrFeNi coatings have been fabricated and evaluated [24, 25]. Extensive studies have examined its microstructure in

the as-cast state [26–28] and after heat treatment [26, 29–31], alongside assessments of their corrosion resistance [32], physical properties [33], and mechanical characteristics such as hardness [3], compressive strength [34], erosion resistance [35, 36], and tensile strength [37]. Research has also explored their behavior under high temperature oxidation conditions [38–42], including how grain size influences oxidation kinetics [43, 44]. The impact of various alloying elements, such as Nb [45, 46], Hf [47, 48], Y [45, 49], Ta [49], W [50], Si [51], Ti [52], and Mo [21, 53, 54] on the properties of AlCoCrFeNi alloys has been similarly investigated.

As a relatively new class of materials, high entropy alloys still pose many questions that have not yet been fully explored [55-57]. One such issue is understanding how the molybdenum (Mo) content influences the microstructure and hightemperature stability of the AlCoCrFeNi HEA. Studies by Gopal et al. [21] and Zhu et al. [53] have examined how the addition of Mo affects the microstructure and mechanical properties of this alloy. They observed that, in the as-cast state, alloys with Mo concentrations exceeding 0.1 mol% typically exhibit a lamellar eutectic microstructure consisting of two phases: a NiCoAlrich BCC phase and a MoCrFe-rich α phase. An increase in tensile strength was observed, often accompanied by a reduction in ductility. Studies in the literature indicate that alloying elements such as Mo are employed to enhance creep resistance in nickel superalloys, as they improve hightemperature mechanical performance through solution strengthening and precipitation effects. However, Ni superalloys are vulnerable to high temperature corrosion, and Mo itself tends to form volatile oxides under such conditions, leading to rapid oxidation.

Therefore, the aim of the present research is to investigate the effect of Mo addition on the microstructure, mechanical properties, and high-temperature oxidation resistance of the Al-CoCrFeNi-based high entropy alloy.

EXPERIMENTAL

In the present work, we developed high entropy alloys based on the AlCoCrFeNi system with equiatomic content of each element alloyed with Mo from 1 to 5 at.% with 1 at.% step are studied. The projected chemical compositions of

studied HEA are given in Table 1. To simplify the alloy, AlCoCrFeNi will be designed as Ref., Al-CoCrFeNi + 1 at%. Mo - Ref.+1Mo, AlCoCrFe-Ni + 2 at%. Mo – Ref.+2Mo, AlCoCrFeNi + 3 at%. Mo - Ref.+3Mo, AlCoCrFeNi + 4 at%. Mo – Ref.+4Mo and AlCoCrFeNi + 5 at%. Mo - Ref.+5Mo. HEA were produced by arc melting. In the first step, high purity powders (purity > 99.99%) were weighted in the appropriate proportions, mixed in the ball mill to ensure uniform distribution of powders, and finally pressed into the form of cylinders with a diameter of 12 mm and a height of 15 mm. These prepared pellets were placed in the vacuum chamber of the arcmelter. Prior melting air was evacuated from the chamber and purged with 5N purity argon gas to remove air remnants. After 5 repetitions of Ar purging, a melting process was performed. After the pellets each of them was reversed and remelted five times to ensure uniform chemical composition of the cast alloys. After melting, the alloys were cooled down with the furnace in the atmosphere of Ar. Cross sections of such alloy cross sections were prepared for investigation of the chemical composition, microstructure, and microhardness of the products manufactured under as-cast conditions. Phase analysis was conducted utilizing X-ray diffraction (XRD) with a Mini-flex II X-ray diffractometer manufactured by Rigaku. An X-ray source was provided by a copper lamp (CuK α , $\lambda = 0.1542$ nm) operated at 40 kV. The diffraction data was collected over a 20 range of 20 ° to 100°, with a scanning step size of 0.02 ° per second. The rest of the material was cut to prepare rectangular specimens with dimensions of $8 \times 12 \times 2$ mm for isothermal oxidation tests. The sample surface was ground to 1200 grit SiC papers. After grinding, the samples were ultrasonically cleaned with ethanol and dimensions and mass of samples were measured. These prepared samples were subjected to isothermal air oxidation tests at 1000 °C for 24, 100 and 1000 hours of exposure. Two samples per each studied material were exposed parallel to ensure reproducibility of the results obtained. After oxidation, the samples were weighted to calculate the oxidation kinetics of the studied materials. The oxidized specimens were subjected to surface analysis using scanning electron microscopy (SEM). Selected specimens were investigated using glow discharge optical emission spectrometry (GD-OES) in terms of element distribution as a function of sputtering time (indirectly as a function of depth). GD-OES depth

profiles were quantified using relative sensitivity factors (RSF) according to the procedure described elsewhere [58–60]. After GD-OES analysis, samples were electroplated with Ni and cross sections of the oxidized materials were prepared according to standard metallographic procedures. Cross sections were observed using SEM.

RESULTS AND DISCUSSION

As-cast conditions

Tables 1 and 2 show the designed and measured chemical compositions of the investigated HEA. The chemical composition of HEA was designed to be equiatomic for the main alloying elements, i.e., Al, Co, Cr, Fe and Ni, and variation in the Mo content was planned with step 1 at.% (Table 1). As shown in the measured chemical composition, most of the measured elements are close to those designed ones. The only exception is Al, which shows slightly lower content than the designed one (Table 2). The most probable reason for such a phenomenon is the fact that Al has the lowest melting temperature among all elements used (about 660 °C), while its boiling temperature is 2519 °C. Since the temperature during arc melting can easily reach a temperature above 3000 °C, evaporation of part of Al is likely to occur. However, the differences are not higher than 1-1.8 at.%. Thus, one can conclude that there is

good agreement between the designed and measured chemical composition of the studied materials. Figures 1 and 2 show the microstructure of the studied HEA taken at low magnification (Figure 1) and high magnification (Figure 2). The microstructures shown in Figure 1 reveal that the increase in addition of Mo causes changes in the microstructure from regular grains (Figure 1a) to transformation towards formation of dendrites (Figures 1b to 1f). Meanwhile, images taken at high magnification revealed that the increase in Mo content caused an increase in microstructural ordering from lamellar (Figure 2a) to mosaic-like structures (Figures 2b – 2f)). Such a mosaic structure was observed especially in the case of HEA containing 4 at.% of Mo (Figure 2e) and 5 at.% of Mo (Figure 2f). The SEM/EDS elemental map shown in Figure 4 revealed a rather uniform distribution of the alloying elements. However, it are observed that Al and Ni is enriched in the darker phase, while Co, Cr, Fe, and Mo are enriched in the lighter one (Figure 3).

The results of the phase analysis of HEA under the as-cast conditions are shown in Figure 4. The results obtained showed that Ref. The alloy consists of the BCC-B2 phase. Addition of 1 to 5 at.% of Mo leads to formation of sigma phase, while for HEA containing 4 and 5 at.% of Mo an additional peak is found characteristic for μ phase is found. Thus, the conclusion is that the addition of Mo significantly alters the phase composition of the studied HEA.

Table 1. Projected chemical composition of the studied HEA (in at.%)

Element	Co	Ni	Al	Cr	Fe	Мо	HEA designation
	20.0	20.0	20.0	20.0	20.0	0.0	Ref.
	19.8	19.8	19.8	19.8	19.8	1.0	Ref.+1Mo
Concentration at.%	19.6	19.6	19.6	19.6	19.6	2.0	Ref.+2Mo
	19.4	19.4	19.4	19.4	19.4	3.0	Ref.+3Mo
	19.2	19.2	19.2	19.2	19.2	4.0	Ref.+4Mo
	19.0	19.0	19.0	19.0	19.0	5.0	Ref.+5Mo

Table 2. Chemical composition of HEA studied measured by SEM/EDS (in at.%)

Element	Co	Ni	Al	Cr	Fe	Мо	HEA designation
	20.2	20.8	18.2	20.3	20.4	0.0	Ref.
	21.2	19.4	18.5	20.3	19.5	1.1	Ref.+1Mo
Concentration at.%	19.6	19.7	18.8	20.2	19.8	1.9	Ref.+2Mo
	18.0	19.9	18.1	20.7	20.1	3.0	Ref.+3Mo
	19.4	19.6	18.5	19.3	19.3	4.0	Ref.+4Mo
	19.3	18.7	18.1	18.5	19.0	5.4	Ref.+5Mo

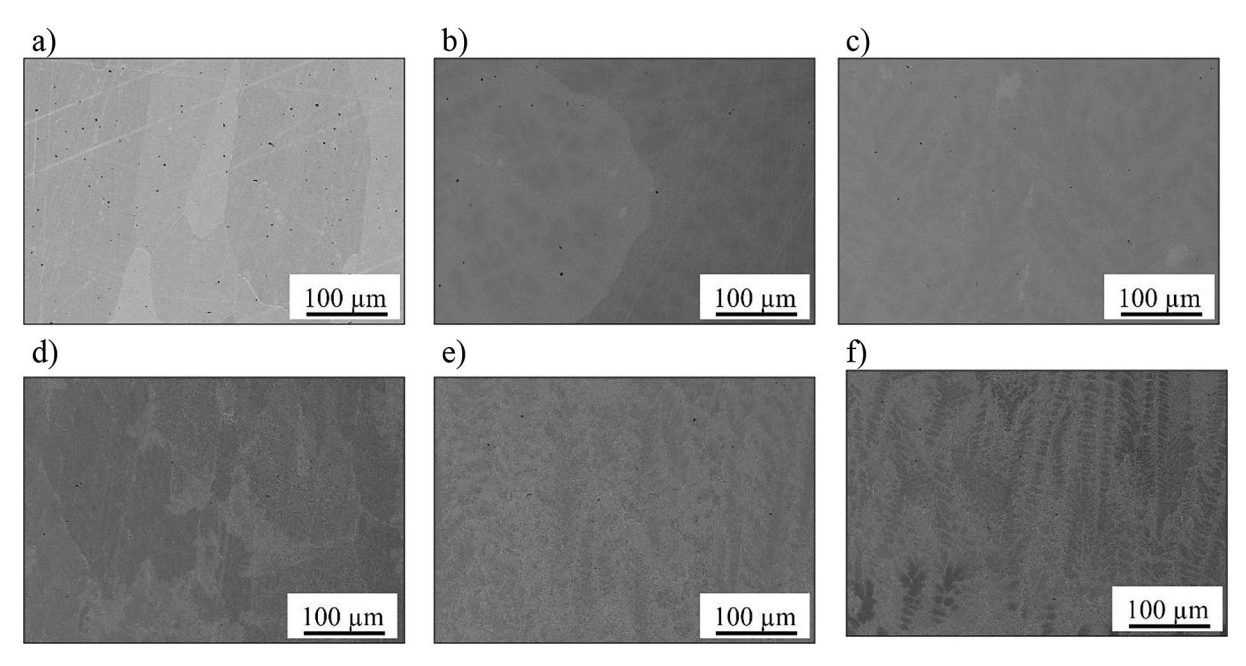


Figure 1. SEM/BSE images of studied alloys in the as cast conditions taken for: a) Ref., b) Ref.+1Mo, c) Ref.+2Mo, d) Ref.+3Mo, e) Ref.+4Mo, f) Ref.+5Mo taken at low magnification

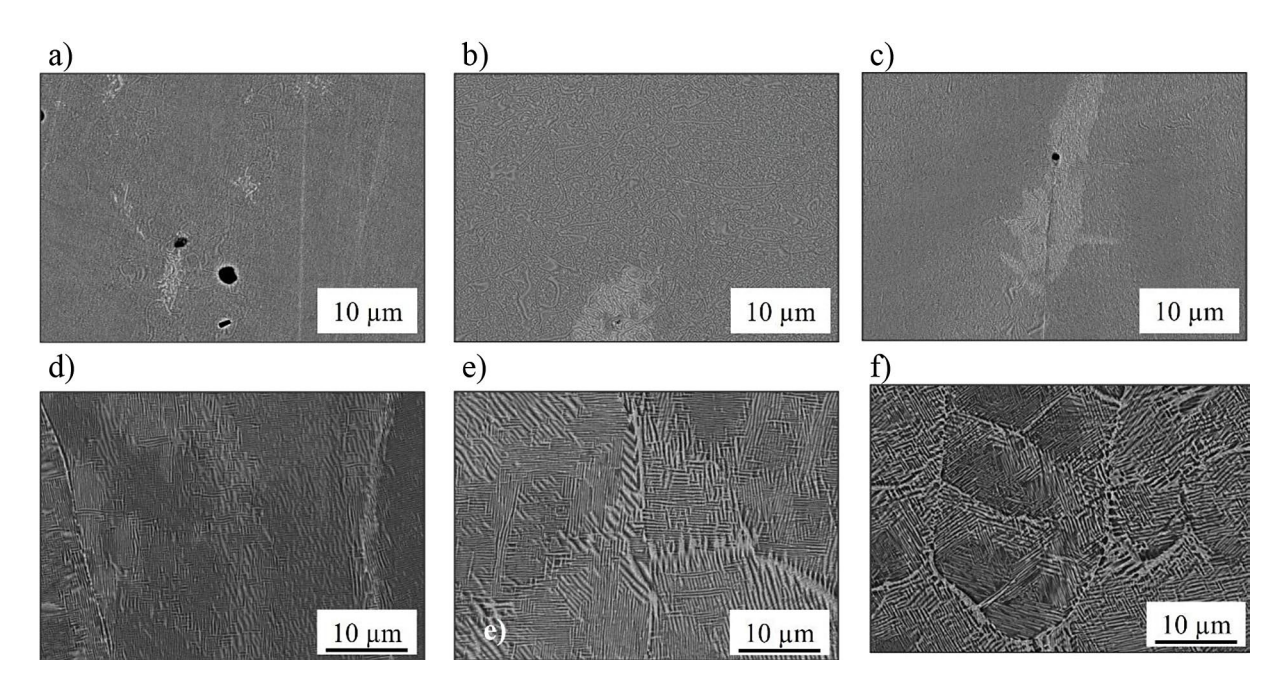


Figure 2. SEM/BSE images of studied alloys in the as cast conditions taken for: a) Ref., b) Ref.+1Mo, c) Ref.+2Mo, d) Ref.+3Mo, e) Ref.+4Mo, f) Ref.+5Mo taken at high magnification

In addition to XRD phase analysis thermodynamic calculations using ThermoCalc software was employed to calculate the phases stabilities for the studied HEA. As is visible in plots in Figure 5 Ref. The HEA presence of two phases was calculated, namely BCC_B2#1 and BCC_B2#3. Addition of Mo to Ref. HEA at any concentration causes formation of two additional phases, namely μ -phase and

 σ -phase. The composition of the mentioned phases is shown in Table 3. The presence of all four mentioned phases is visible for each Mo concentration; however, volume fraction of the phases changes with increasing Mo content (Table 4). Namely, an increase in Mo content causes a decrease a the BCC volume fraction and in parallel increase in μ-phase and σ -phase volume fraction (Table 4).

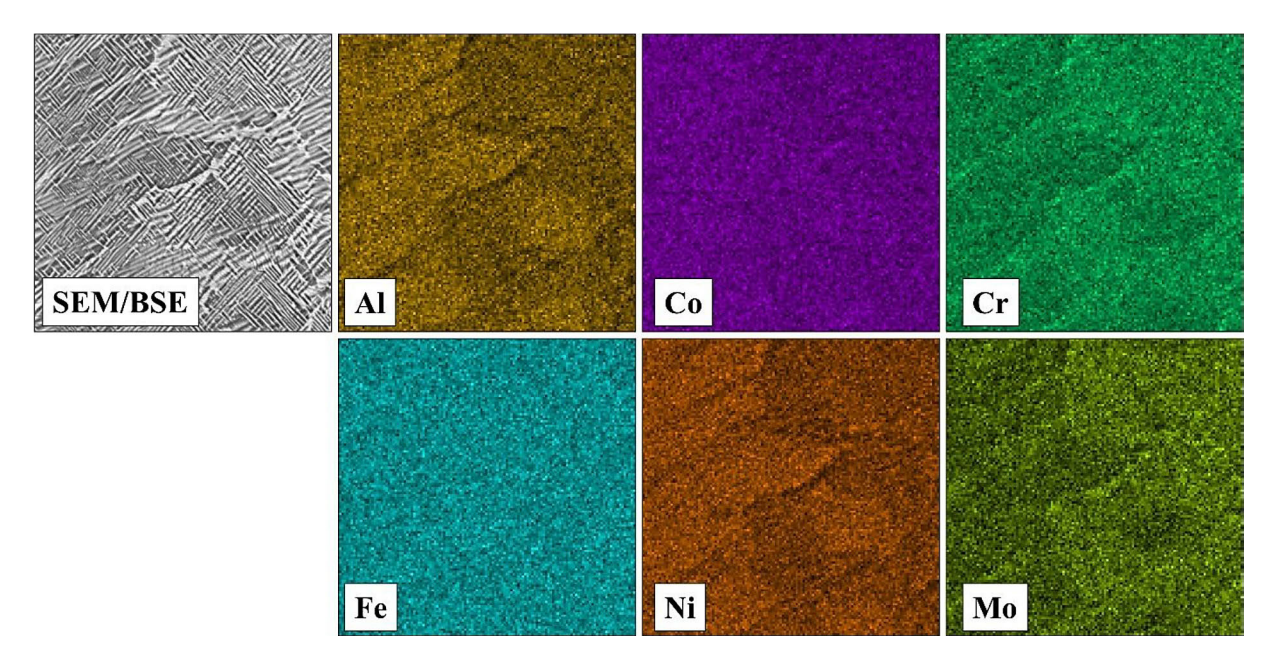


Figure 3. SEM elemental mapping showing distribution of elements for observed Ref.+5Mo

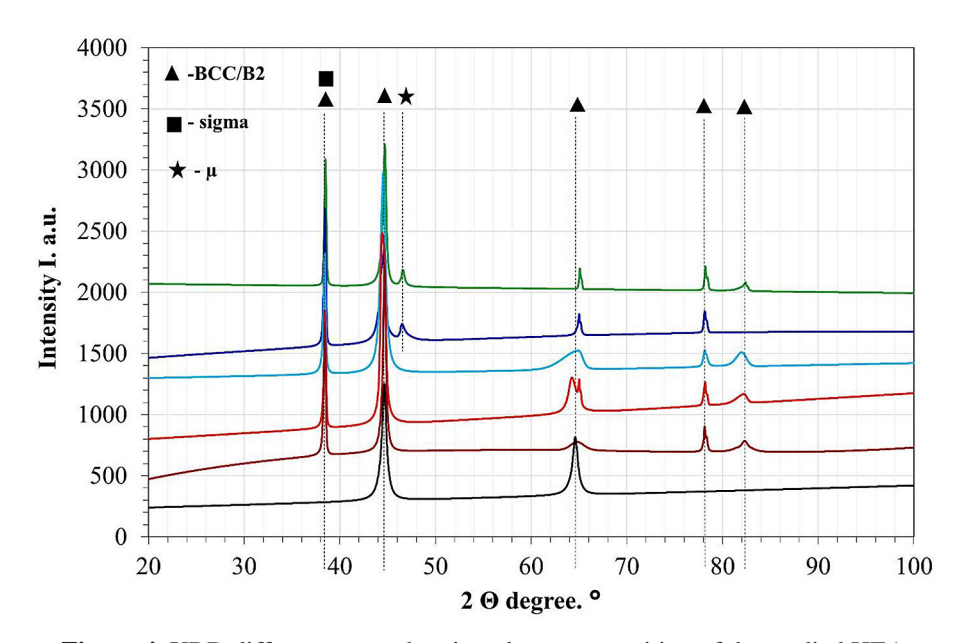


Figure 4. XRD diffractograms showing phase composition of the studied HEA

On samples in the as-cast condition, microhardness measurement has been performed. The results obtained are shown in Figure 6. Measured microhardness of Ref. and Ref.+1Mo is about the same level. A slight increase of about 6% in microhardness is observed for Ref.+2Mo and HEA +3Mo. However for Ref.+4Mo and Ref.+5Mo a significant increase (about 50%) in microhardness is observed. Similar observation was made in the work of Walczak et al. [61]. Thus, Mo addition in the amount equal to or

greater than 4 at.% leads to hardening of the studied HEA of about 50% compared to Ref. The most probable reason for such a phenomenon is the change in the HEA microstructure caused by Mo addition. Furthermore, it is assumed that the increase in volume fraction of μ -phase and σ -phase also participates in the increase in microhardness of the studied HEA. Apparently the total content of μ -phase and σ -phase higher than 9% causes a sudden increase in microhardness.

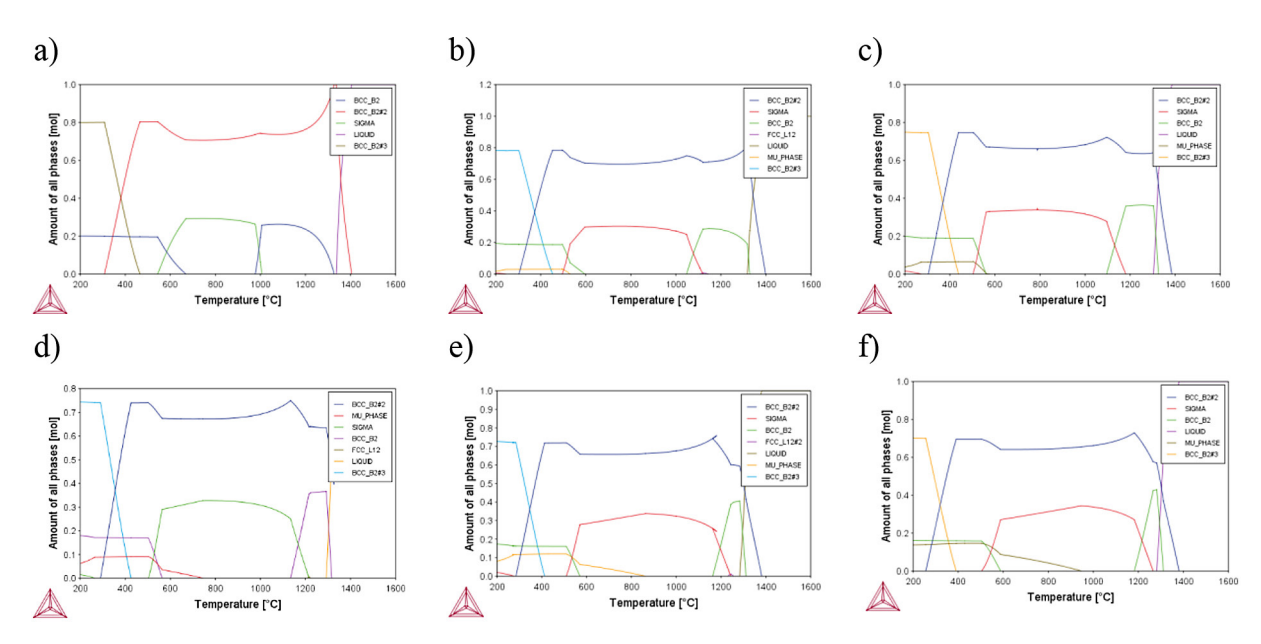


Figure 5. Phase stability diagrams calculated using ThermoCalc for studied HEA: a) Ref., b) Ref.+1Mo, c) Ref.+2Mo, c) Ref.+3Mo, d) Ref.+4Mo and d) Ref.+5Mo

Table 3. Chemical composition of calculated phases present in studied alloys (in at. %)

Phase	Element concentration in at. %							
	Al	Co	Cr	Fe	Ni	Мо		
BCC_B2#1	-	-	99.64	0.36	-	-		
BCC_B2#3	25	25	-	25	25	-		
μ		17.5	21	25.5	-	36		
σ#1	-	-	13.5	1.1	32.2	53.2		

Table 4. Volume fraction of phases calculated for studied alloys (in %)

Phase	Volume fraction, %							
	Ref.	Ref.+1Mo	Ref.+2Mo	Ref.+3Mo	Ref.+4Mo	Ref.+5Mo		
BCC_B2#1	21	20	21	18	18	17		
BCC_B2#3	79	77	73	73	71	69		
μ	0	2	4	7	9	11		
σ#1	0	1	2	2	2	3		

Air oxidation tests

Normalized mass changes obtained during air exposure of the studied HEA at 1000 °C for 24, 100 and 1000 hours are shown in Figure 7. The results obtained show that the lowest mass change after 1000 h, which is equal to 0.65 mg·cm² is observed for the reference material Ref. Interestingly, the addition of Mo causes an increase in the total mass change after 1000 h for 0.82, 0.92, 1.1, 1.3 and 2.0 mg·cm² for Ref.+0.1Mo, Ref.+0.2Mo, Ref.+0.3Mo, Ref.+0.4Mo and Ref.+0.5Mo respectively. It

is also worth noting that the oxidation kinetics changes from nearly parabolic for Ref. to almost linear for Ref.+5Mo. Such a change in the mass change curves is observed continuously for materials with increasing Mo content.

SEM/BSE images of the surface of air-oxidized HEA are shown in Figure 8. As can see in the samples exposed for 24 hours, a pure ${\rm Al_2O_3}$ oxide scale is developed. However, for some alloys, severe oxide scale spallation is already found after 100 hours (Figure 9). The formation of the alumina scale causes the depletion of

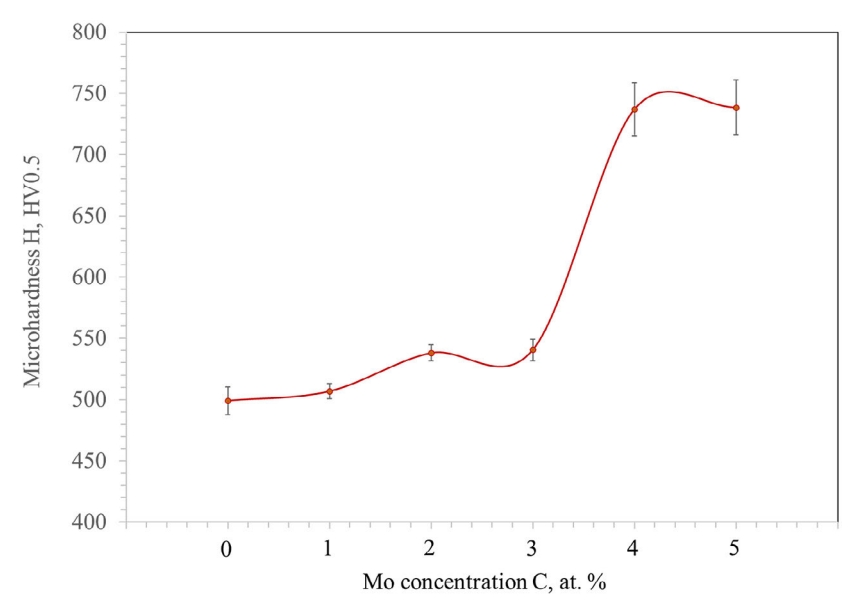


Figure 6. Results of microhardness tests obtained for the HEA studied HEA with variation of the Mo content

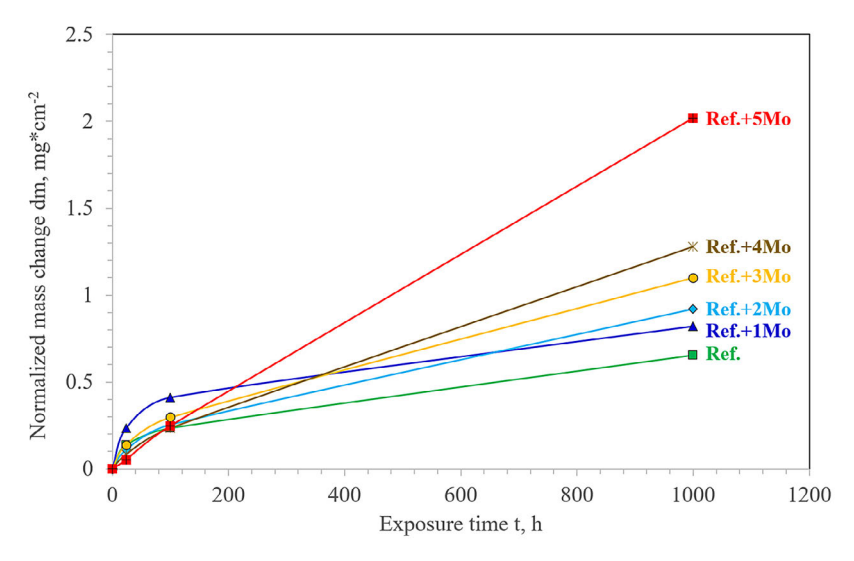


Figure 7. Normalized mass change obtained for the studied HEA with variation of Mo content during air exposure at 1000 °C up to 1000 h

Al from the near-surface region, which is naturally enriched in other alloying elements. The phenomenon of spallation of the alumina scale causes direct exposure of Al-depleted metal to the the oxidant and leads to formation of non-protective oxides based on Ni/Cr/Fe/Co spinels, as shown in surface images of the studied HEA after 100 hours of exposure (Figure 8). According to Wagner's theory, there is a minimum Al concentration to form an external oxide scale [62]. Apparently, after 100 hours of exposure, the Al content in the Al-depleted zone was not enough to form a continuous external Al₂O₃ oxide scale, especially considering the relatively high Ni, Cr,

Co, and especially Fe content in the near-surface Al-depleted zone. SEM/BSE images of HEA the surfaces of studied after 1000 h reveal an increased area of spinels islands for alloys with an increased Mo content. This situation is shown in the example of the elemental map (Figure 10). This can partially explain the transition from parabolic to nearly linear oxidation law. Therefore, the addition of Mo to the studied HEA worsens its oxidation resistance. The formation of a pure alumina scale is supported by GD-OES depth profiles performed on samples after exposure for 24 hours. The results obtained showed in external oxide scale coenrichment of oxygen and Al

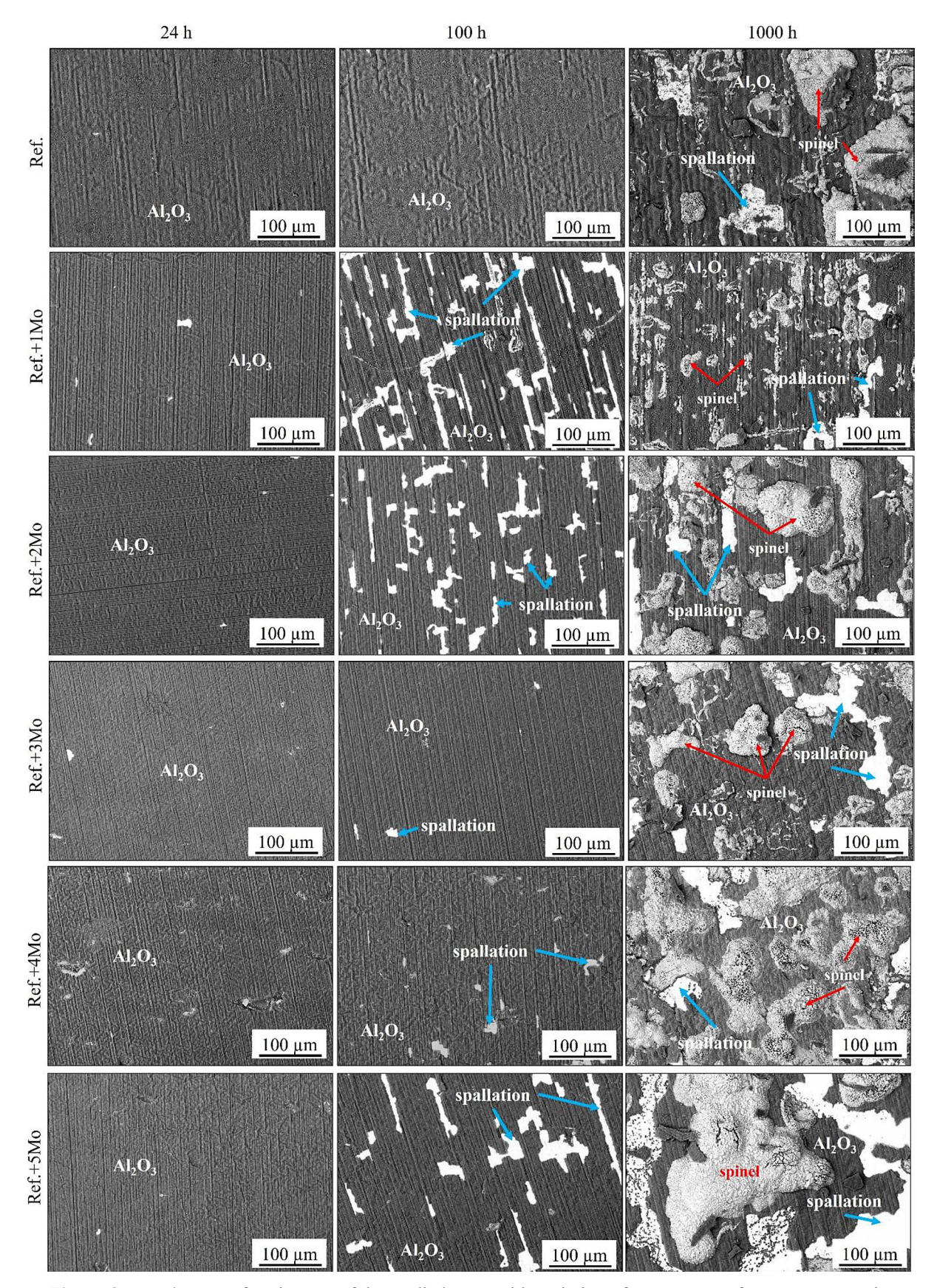


Figure 8. SEM/BSE surface images of the studied HEA with variation of Mo content after exposure to air at $1000 \,^{\circ}\text{C}$ up to $1000 \,\text{h}$

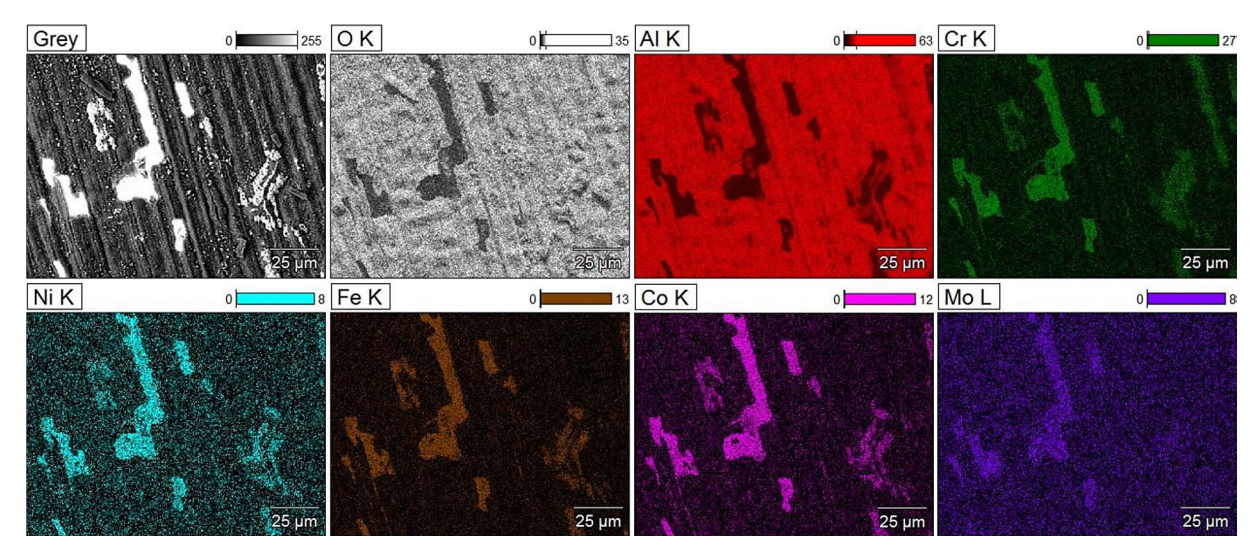


Figure 9. SEM/EDS elemental map of the surface of Ref.+3Mo after air exposure at 1000 °C for 100 h

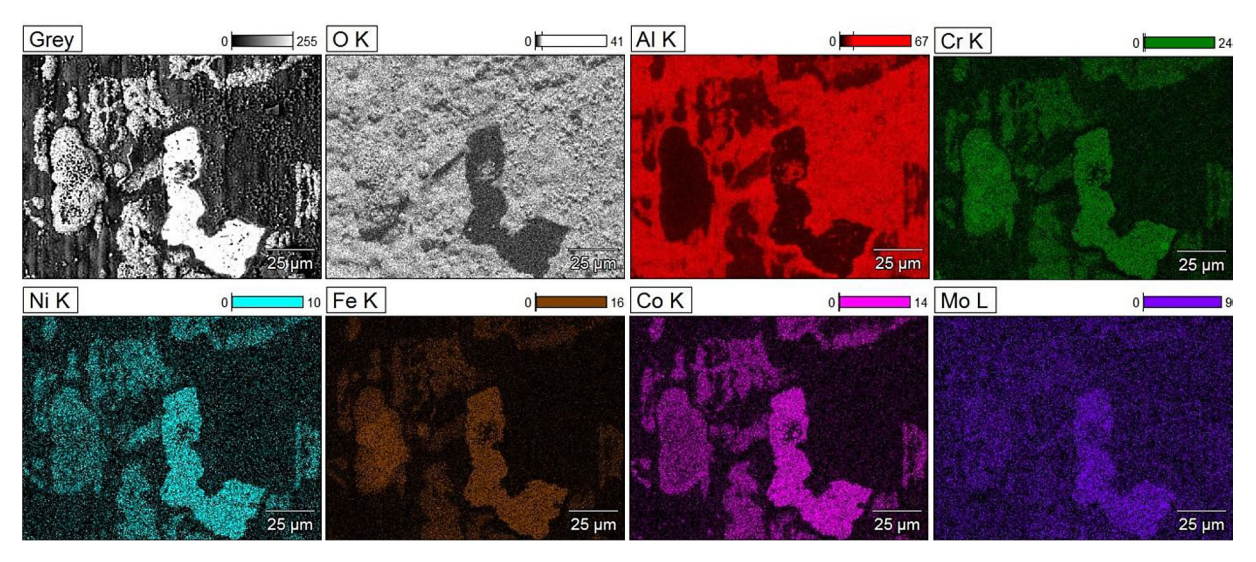


Figure 10. SEM/EDS elemental map of the surface of Ref.+3Mo after air exposure at 1000 °C for 1000 h

is present, what clearly showing the formation of pure alumina scale (Figure 11). It was also observed that after 24 hours of exposure, Mo does not actively participate in oxide scale formation. This statement is supported by observation of the Mo profile, which in the region of external oxide scale is relatively low (Figure 11 b-f).

SEM/BSE analyzes of the cross sections of studied after air exposure up to 100 hours are shown in Figure 12. As shown in the cross sections after exposure for 24 hours, a thin Al₂O₃ oxide scale is formed in the case of all of the alloys studied. However, after 10 hours of exposure, severe oxide scale cracking is observed

and also in the case of some HEA formation of spinels already after 100 hours of exposure is found. The latter can be caused by earlier oxide scale cracking/spallation, as shown in Figure 8, and small areas where the alumina scale spalled off and consequently exposed Al-depleted HEA to air can be raised as the reason for the observed phenomenon. The Al depletion zone is clearly visible already after 24 hours of exposure in the GD-OES depth profiles, on which a decrease in Al concentration is observed just after the external oxide scale (Figure 11 a-f). However, as shown in Figure 8, most of the alloys studied revealed alumina scale spallation after 100 h of

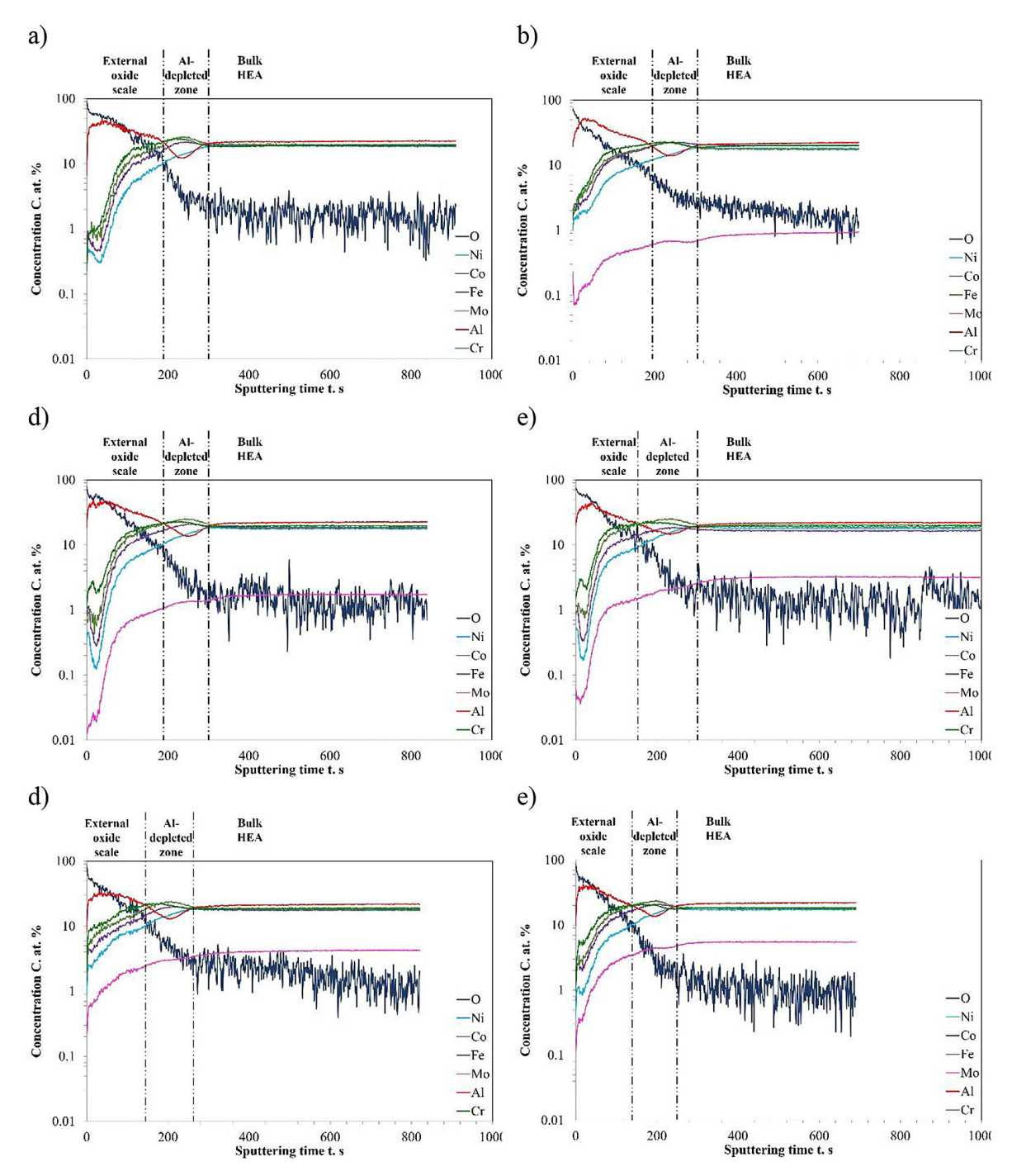


Figure 11. GD-OES depth profiles performed on: a) Ref., b) Ref.+1Mo, c) Ref.+2Mo, d) Ref.+3Mo, e) Ref.+4Mo, f) Ref.+5Mo after air exposure at 1000 °C for 24 hours

exposure, leading to severe oxidation on top of exposed Al-depleted HEA exposed. After alumina scale spallation, Al-depleted HEA was exposed to oxidation in air. This means that the alloy was exposed to not only oxygen from air but also to nitrogen. It was found that the diffusion coefficient for nitrogen was one order of magnitude higher than for oxygen in Co-based alloys [63], therefore it is highly possible that

a similar situation is found for systems studied containing 20 % of Co similar situation is found. Therefore, it is believed that after the spallation of the alumina scale, nitrogen diffuses first and reacts with Al, forming internal precipitates of AlN and the same blocking further outward diffusion of Al to form an external alumina scale. Such a situation is confirmed in SEM/EDS elemental maps shown in Figures 13 a) and b).

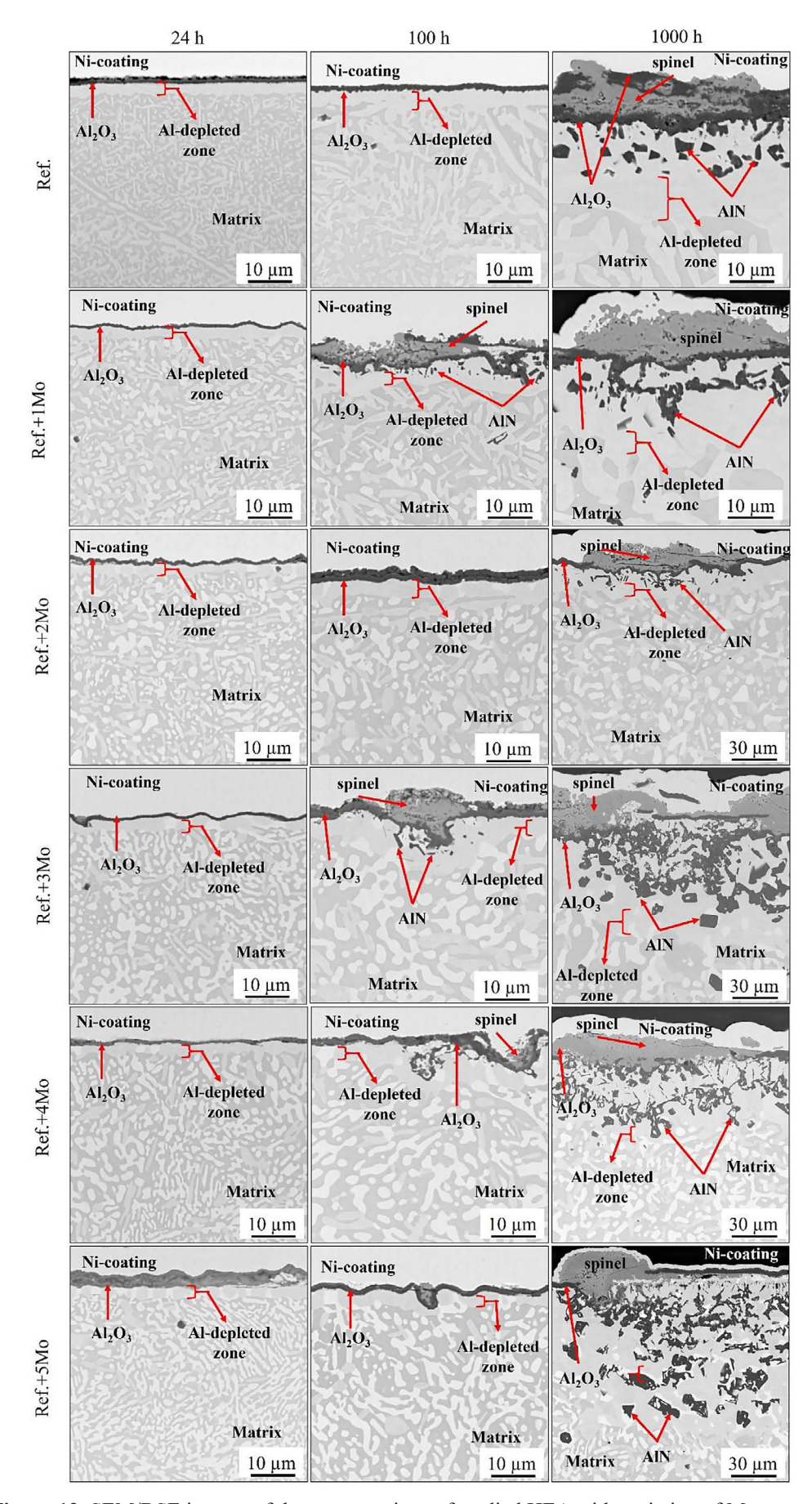


Figure 12. SEM/BSE images of the cross sections of studied HEA with variation of Mo content after air exposure at 1000 °C up to 1000 h

This oxidation mechanism is found for each alloy studied. However, as shown in Figure 14, an increase in Mo content caused an increase in the internal nitridation zone. This effect can be correlated with an increase in the volume fraction of Mo-rich phases i.e. μ and σ (Tables 3 and 4). Even if alumina scales form initially, after cracking and/or spalling off the alumina scale, nitrogen penetrates first, leading to successive blocking of Al-flux by entrapping Al in the form of AlN and causes formation of Ni/Cr/Fr/

Co-spinels. The oxidation mechanism described above is shown schematically in Figure 15. The PBR of these spinels is higher than the PBR of the alumina scale; thus, its formation leads to further cracking of the formed alumina scale, as observed in Figure 12. Therefore, in the present work, it is claimed that an increase in the Mo content, despite a significant increase of HEA, causes also worsening of the oxidation resistance of the studied HEA during exposure in dry air (Figure 13, 14).

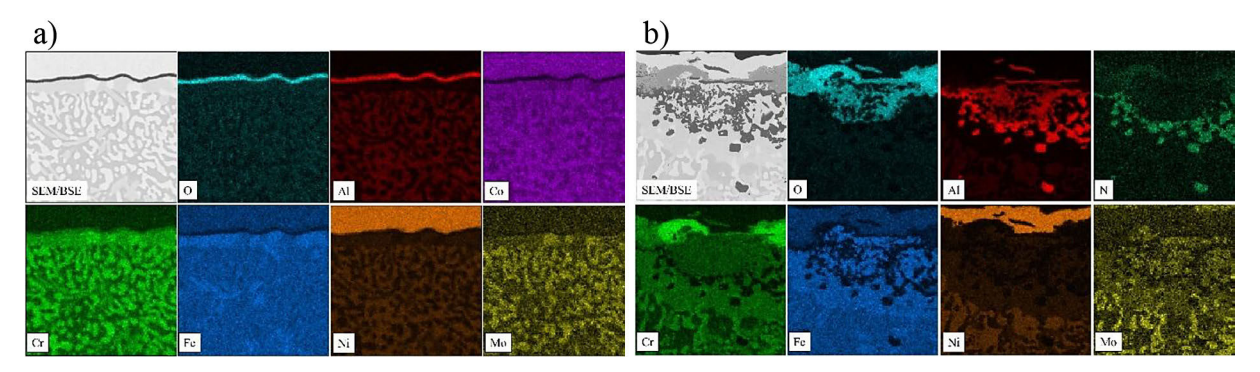


Figure 13. SEM/EDS elemental maps obtained for Ref.+3Mo after air oxidation at 1000 °C for: a) 24 hours and b) 1000 h

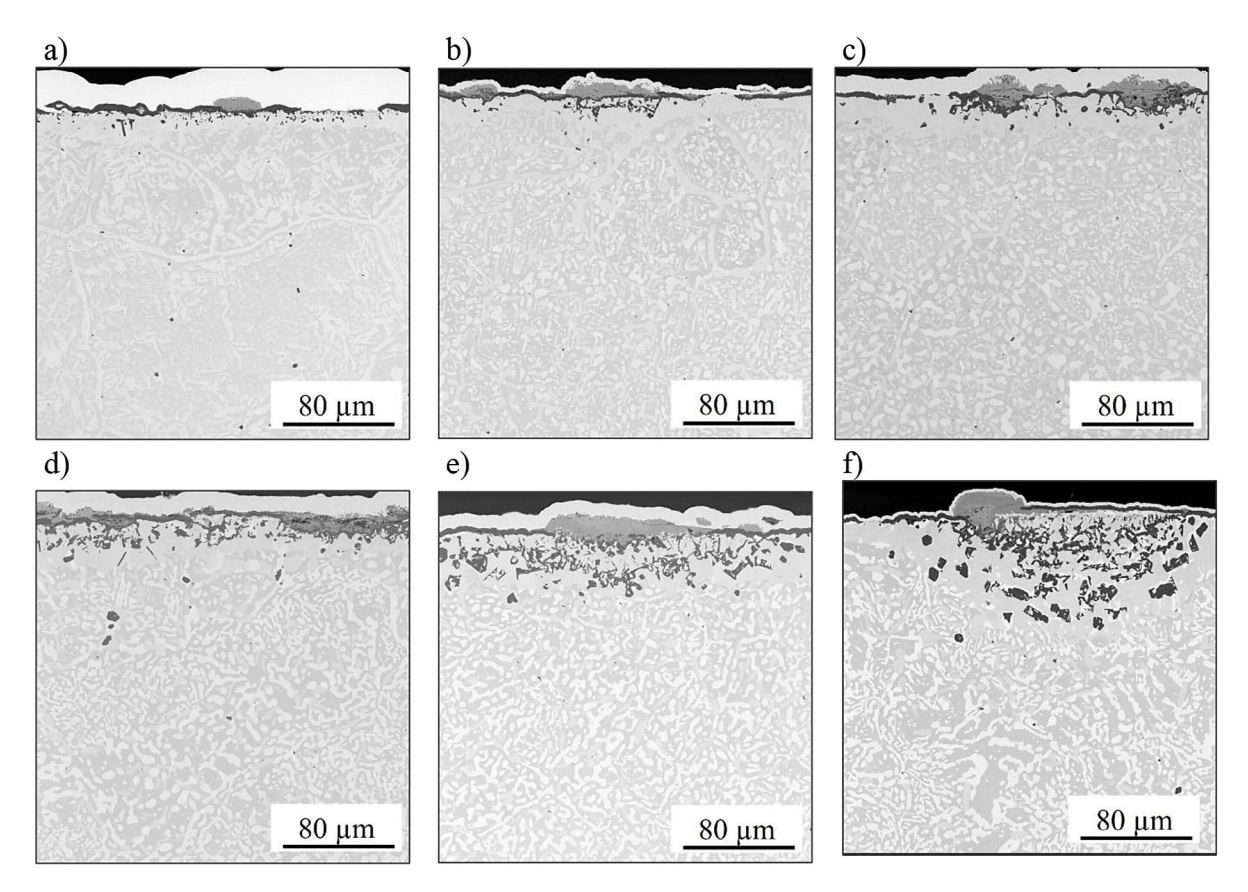


Figure 14. SEM/BSE images of the cross sections of studied HEA after air exposure at 1000 °C up to 1000 h with: a) 0, b) 1, c) 2, d) 3, e) 4 and f) 5 at.% of Mo

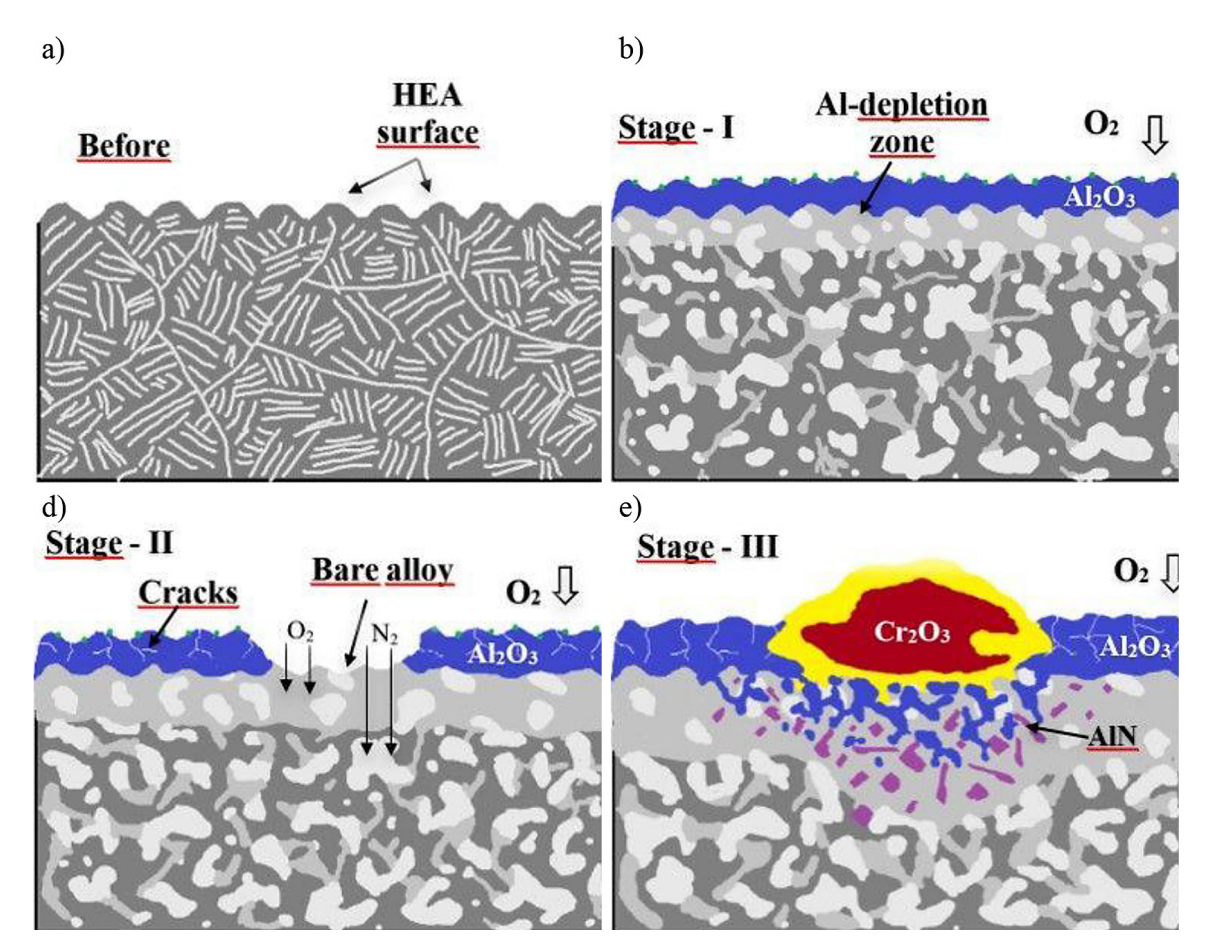


Figure 15. Schematic representation of oxidation mechanism for studied HEA

CONCLUSIONS

Based on the results, the following conclusions can be drawn:

- The increase in Mo content from 0 to 5 at.% causes severe changes in the AlCoCrFeNi-Mo_x
 HEA microstructure. The higher the Mo content, the more organized the form of mosaic is obtained.
- 2. Increasing the Mo content in the studied HEA causes the formation of σ phase and μ phase formation is also found for alloys containing 4 and 5 at% of Mo.
- 3. Increasing the Mo content in the studied HEA causes a slight increase in microhardness for the case of the addition of 1–3 at.% of Mo. However, the addition of 4 and 5 % Mo into the studied HEA caused an increase in microhardness of about 50%. As a reason for this phenomenon, formation of the mosaic structure was claimed.
- 4. No direct correlation was found between HEA microhardness and oxidation resistance.
- 5. The increase in Mo content in the AlCoCrFeNi

HEA case caused a worsening of oxidation resistance during air oxidation tests at 1000 °C until 1000 h. As a reason for this phenomenon, alumina scale spallation and formation of internal AlN precipitates were claimed. The formation of AlN species f mentioned above effectively blocked the outward diffusion of Al and prevented the formation of protective external alumina scale.

6. The depth of the internal nitridation zone increases with the increase in the Mo content; thus, the conclusion is that the increase in the Mo content decreases the air oxidation resistance of the studied HEA.

Acknowledgments

The authors thank Dr. Kamil Gancarczyk for recording the XRD data. Expressions of gratitude are also addressed to M.Sc. Grzegorz Jakubowicz, M.Eng., for performing microhardness measurements. This research was funded in whole by the National Science Centre, Poland, Grant No. 2020/39/B/ST8/00334.

REFERENCES

- 1. Williams J. C., Starke E. A. Progress in structural materials for aerospace systems, Acta Materialia, 2003; 51: 5775–5799.
- 2. Rapp R. A., Devan J. H., Douglass D. L., Nordine P. C., Pettit F. S., Whittle D. P. High temperature corrosion in energy systems, Materials Science and Engineering. 1981; 50: 1–17.
- 3. Beele W., Marijnissen G., van Lieshout A. The evolution of thermal barrier coatings status and upcoming solutions for today's key issues. Surface Coatings and Technology. 1999; 120–121: 61–67.
- 4. Lapin J. Hradec nad Moravicí, in TiAl-based Alloys: Present Status and Future Perspectives, 19–21. 5. 2009
- Reed R. C., The Superalloys: Fundamentals and Applications, New York: Cambridge University Press, 2006.
- 6. James A. W., Rajagopalan S., Gas turbines: operating conditions, components and material requirements, w Structural Alloys for Power Plants, Sawston, Woodhead Publishing, 2014; 3–21.
- DeMasi-Marcin J. T., Gupta D. K. Protective coatings in the gas turbine engine. Surface and Coatings Technology. 1994; 68/69: 1–9.
- 8. Liu X., Wang T., Li C., Zheng Z., Li Q. Microstructural evolution and growth kinetics of thermally grown oxides in plasma sprayed thermal barrier coatings. Progress in Natural Science Materials International. 2016; 26: 103–111.
- Gancarczyk K., Albrecht R., Kawalec M., et al. The effect of re content on microstructure and creep resistance of single crystal castings made of nickelbased superalloys. Advances in Science and Technology Research Journal. 2024; 18(1): 291–305. https://doi.org/10.12913/22998624/178463
- Stroosnijder M. F., Mevrel R., Bennett M. J. The interaction of surface engineering and high temperature corrosion protection, Materials at High Temperatures. 1994; 12: 53–66.
- 11. Meier G. H. A review of advances in high-temperature corrosion. Materials Science and Engineering. 1989; A120: 1–11.
- 12. Singh K. Advanced materials for land based gas turbines. Transactions of the Indian Institute of Metals. 2014; 67: 601–615.
- 13. Hu D., Miller R. A., Fox D. S. Thermal and Environmental Barrier Coating Development for Advanced Propulsion Engine Systems, in 48th AIAA/ASME/ASCE/AHS/ASC Structures, Structural Dynamics, and Materials Conference, Honolulu, 2007.
- 14. Schutze M., Quadakkers W. J. Future directions in the field of high-temperature corrosion research. Oxidation of Metals. 2017; 87: 681–704.

- 15. Nowak W. J., Wierzba B., Mazurkow A., Jaworski A., Krawczyk Ł. Increase of austenitic ductile iron type D5S durability by high temperature pre-treatment. Journal of Mining and Metallurgy, Section B: Metallurgy. 2020; 56: 353–360.
- 16. Chen J., Zhou X., Wang W., Liu B., Lv Y., Yang W., Xu D., Liu Y. A review on fundamental of high entropy alloys with promising high temperature properties. Journal of Alloys and Compounds. 2018; 760: 15–30.
- 17. Tsai M. H., Yeh J. W. High entropy alloys: A Critical Review. Materials Research Letters. 2014; 2: 107–123.
- 18. Miracle D. B., Miller J. D., Senkov O. N., Woodward C., Uchic M. D., Tiley J. Exploration and Development of High Entropy Alloys for Structural Applications. Entropy. 2014; 16: 494–525.
- 19. Cantor B. Multicomponent and High Entropy Alloys. Entropy. 2014; 16: 4749–4768.
- 20. George E. P., Raabe D., R. Ritchie O. High entropy alloys. Nature Reviews Materials. 2019; 4: 516–534.
- 21. Gopal P. M., Prakash K. S., Kavimani V., Rajendiran G. Processing and Properties of AlCoCrFeNi High Entropy Alloys: A Review. Advances in Materials Science and Engineering. 2022; 1–13.
- 22. Alvi S. A. Synthesis and Characterisation of High Entropy Alloy and Coating, Lulea: Lulea University of Technology. Graphic Production. 2019.
- 23. Rogal Ł., Szklarz Z., Bobrowski P., Kalita D., Garzeł G., Tarasek A., Kot M. i Szlezynger M. Microstructure and Mechanical Properties of Al–Co–Cr–Fe–Ni Base High Entropy Alloys Obtained Using Powder Metallurgy. Metals and Materials International. 2019; 25: 930–945.
- 24. Meghwal A., Singh S., Anupam A., King H. J., Schulz C., Hall C., Munroe P., Berndt C. C., Ming Ang A. S. Nano- and micro-mechanical properties and corrosion performance of a HVOF sprayed Al-CoCrFeNi high entropy alloy coating. Journal of Alloys and Compounds. 2022; 912: 1–16.
- 25. Zhang F., Wang L., Yan S., Yu G., Chen J., Yin F. High temperature oxidation behavior of atmosphere plasma sprayed AlCoCrFeNi high entropy alloy coatings. Materials Chemistry and Physics. 2022; 282: 1–12.
- 26. Zhang Y., Zuo T. T., Gao M. C., Dahmen K. A., Liaw P. K., Lu Z. P. Microstructures and properties of high entropy alloys. Progress in Materials Science. 2014; 61: 1–93.
- 27. Wang Y. P., Li B. S., Ren M. X., Yang C., Fu H. Z. Microstructure and compressive properties of AlCrFeCoNi high entropy alloy. Materials Science and Engineering A. 2008; 491: 154–158.
- 28. Shun T. T., Du Y. C. Microstructure and tensile behaviors of FCC Al0.3CoCrFeNi high entropy

- alloy. Journal of Alloys and Compounds. 2009; 479: 157–160.
- 29. Zhang X., Liu L., Yao K., Duan K., Wu F., Zhao R., Zhang Y., Shang J., Chen M. The phase composition characteristics of AlCoCrFeNi high entropy alloy heat-treated by simple normalizing treatment and its effects on mechanical properties. Journal of Alloys and Compounds. 2022; 926: 1–8.
- 30. Tang Z., Senkov A. N., Parish C. M., Zhang C., Zhang F., Santodonato L. J., Wang G., Zhao G., Yang F., Liaw P. K. Tensile ductility of an AlCoCrFeNi multi-phase high entropy alloy through hot isostatic pressing (HIP) and homogenization. Materials Science & Engineering A. 2015; 647: 229–240.
- 31. Liang L. T., Cheng K. C., Chen S. H. Effect of heat treatment on the phase evolution and mechanical properties of atomized AlCoCrFeNi high entropy alloy powders. Journal of Alloys and Compounds. 2019; 803: 484–490.
- 32. Wang M., Shu Q., Shi J., Teng C. L., Wang J., Jin S., Chen S., Qin J., Wang D. Fabrication of hydrophobic AlCoCrFeNi high entropy alloy and superior corrosion resistance to NTO aqueous solution. Journal of Alloys and Compounds. 2022; 915: 1–11.
- 33. Tsai M. H. Physical Properties of High Entropy Alloys. Entropy. 2013; 15: 5338–5345.
- 34. Wang Y. P., Li B. S., Ren M. X., Yang C., Fu H. Z. Microstructure and compressive properties of AlCrFeCoNi high entropy alloy. Materials Science and Engineering A. 2008; 491: 154–158.
- 35. Tokarewicz, M., Gradzka-Dahlke, M., Nowak, W.J., Gradzik, A., Szala, M., Walczak, M. Effect of vanadium addition on the wear resistance of Al0.7CoCrFeNi high entropy alloy. Materials. 2024; 17: 6021.
- 36. Nowak, W.J., Kubaszek, T., Gradzik, A., Grądzka-Dahlke, M., Perkowski, D., Tokarewicz, M., Walczak, M., Szala, M. Effect of Ti doping of Al0.7CoCrFeNi-based high entropy alloys on their erosion resistance by solid particles. Materials, 2025; 18: 3328.
- 37. Shun T. T., Du Y. C. Microstructure and tensile behaviors of FCC Al0.3CoCrFeNi high entropy alloy. Journal of Alloys and Compounds. 2009; 479: 157–160.
- 38. Hu J., Gu C., Li J., Li C., Feng J., Jiang Y. Microstructure and oxidation behavior of the Y/Ta/Hf co-doped AlCoCrFeNi high entropy alloys in air at 1100 °C. Corrosion Science. 2023; 212: 1–14.
- 39. Lu J., Ren G., Chen Y., Zhang H., Li L., Huang A., Liu X., Cai H., Shan X., Luo L., Zhang X., Zhao X. Unraveling the oxidation mechanism of an Al-CoCrFeNi high entropy alloy at 1100 °C. Corrosion Science. 2022; 209: 1–10.
- 40. Peng Z., Sun J., Luan H., Chen N., Yao K., Effect of Mo on the high temperature oxidation behavior of

- Al19Fe20-xCo20-xNi41Mo2x high entropy alloys. Intermetallics. 2023; 155: 1–6.
- 41. Roy I., Ray P. K., Balasubramanian G. Modeling oxidation of AlCoCrFeNi high entropy alloy using stochastic cellular automata. Entropy. 2022; 24: 1–16.
- 42. Zhu J., Lu S., Jin Y., Xu L., Xu X., Yin C., Jia Y. High temperature oxidation behaviours of AlCoCrFeNi high entropy alloy at 1073–1273 K. Oxidation of Metals. 2020; 94: 265–281.
- 43. Garg M., Grewal H. S., Sharma R. K., Gwalani B., Arora H. S. High oxidation resistance of AlCoCrFe-Ni high entropy alloy through severe shear deformation processing. Journal of Alloys and Compounds. 2022; 917: 1–14.
- 44. Garg M., Grewal H. S., Sharma R. K., Arora H. S. Enhanced oxidation resistance of ultrafine-grain microstructure AlCoCrFeNi high entropy alloy. ACS OMEGA. 2022; 7: 12589–12600.
- 45. Ma S. G., Zhang Y. Effect of Nb addition on the microstructure and properties of AlCoCrFeNi high entropy alloy. Materials Science and Engineering A. 2012; 532: 480–486.
- 46. Jiang H., Li L., Ni Z., Qiao D., Zhang Q., Sui H. Effect of Nb on microstructure and properties of Al-CoCrFeNi2.1 high entropy alloy. Materials Chemistry and Physics. 2022; 290: 1–8.
- 47. Lu J., Li L., Chen Y., Liu X., Zhao X., Guo F., Xiao P. Y-Hf co-doped AlCoCrFeNi high entropy alloy coating with superior oxidation and spallation resistance at 1100 °C. Corrosion Science. 2021; 182: 1–13.
- 48. Ren H., Chen R. R., Gao X. F., Liu T., Qin G., Wu S. P., Guo J. J. Phase formation and mechanical features in (AlCoCrFeNi)100-xHfx high entropy alloys: The role of Hf. Materials Science & Engineering A. 2022; 858: 1–10.
- 49. Hu J., Gu C., Li J., Li C., Feng J., Jiang Y. Microstructure and oxidation behavior of the Y/Ta/Hf co-doped AlCoCrFeNi high entropy alloys in air at 1100 °C. Corrosion Science. 2023; 212: 1–14.
- 50. Wu T., Chen Y., Shi S., Wu M., Gui W., Tan Y., Li J., Wu Y. Effects of w alloying on the lattice distortion and wear behavior of laser cladding AlCoCrFeNiWx high entropy alloy coatings. Materials. 2021; 14: 1–12.
- 51. Li Y., Zhang P., Chen Z., Shen B. Oxidation behavior of AlCoCrFeNiSix high entropy alloys at 1100 °C. Corrosion Science. 2021; 190: 1–11.
- Ham G. S., Kim Y. K., Na Y. S., Lee K. A. Efect of Ti addition on the microstructure and high temperature oxidation property of AlCoCrFeNi high entropy alloy. Metals and Materials International. 2021; 27: 156–165.
- 53. Zhu J. M., Fu H. M., Zhang H. F., Wang A. M., Li H., Hu Z. Q. Microstructures and compressive properties of multicomponent AlCoCrFeNiMox alloys. Materials Science and Engineering A. 2010; 527: 6975–6979.

- 54. Peng Z., Sun J., Luan H., Chen N., Yao K. Effect of Mo on the high temperature oxidation behavior of Al19Fe20-xCo20-xNi41Mo2x high entropy alloys. Intermetallics. 2023; 155: 1–6.
- 55. Zhang W., Liaw P. K., Zhang Y. Science and technology in high entropy alloys. Science China Materials. 2018; 61: 2–22.
- 56. Ye Y. F., Wang Q., Lu J., Liu C. T., Yang Y. High entropy alloy: challenges and prospects. Materials Today. 2016; 19: 349–362.
- 57. Yeh J. W. Alloy design strategies and future trends in high entropy alloys. JOM. 2013; 65: 1759–1771.
- 58. Pfeifer J.-P., Holzbrecher H., Quadakkers W. J., Breuer U., Speier W. Quantitative analysis of oxide films on ODS-alloys using MCs+-SIMS and E-Beam SNMS. Fresenius' Journal of Analytical Chemistry. 1993; 346: 186–191.

- 59. Quadakkers W. J., Elschner A., Speier W., Nickel H. Composition and growth mechanisms of alumina scales on FeCrAl-based alloys determined by SNMS. Applied Surface Science. 1991; 52(4): 271–287.
- Nowak W. J. Characterization of oxidized Ni-Based superalloys by GD-OES. Journal of Analytical Atomic Spectrometry. 2017; 32(9): 1730–1738.
- Nowak, W.J., Hader, B., Ochał, K., Wierzba, B. Increase in Oxidation Resistance of MAR M-509 via LA-CVD Aluminizing. Coatings. 2021; 11: 1306.
- 62. Walczak, M., Nowak, W.J., Szala, M. et al. Effect of molybdenum addition on microstructure and behavior of AlCoCrFeNi high entropy alloys in wet environments. Arch. Civ. Mech. Eng. 2025; 25: 205.
- 63. Wagner C. Zeitschrift für Elektrochemie. Berichte der Bunsengesellschaft für physikalische Chemie. 1959; 63: 772.